1   **Revision 1**

2   **Mechanisms of fluid degassing in shallow magma chambers control the**

3   **formation of porphyry deposits**

4   **Zixuan Wang[1, 2, 3], Yuanchuan Zheng[1, 3, *], Bo Xu[1, 2, *], Zengqian Hou[4], Yang**

5   **Shen[5], Aiping Zhang[6], Lu Wang[1], Changda Wu[4], Qingfeng Guo[2]**

6   [1] State Key Laboratory of Geological Processes and Mineral Resources and

7   School of Earth Sciences and Resources, China University of Geosciences,

8   Beijing 100083, People's Republic of China

9   [2] School of Gemology, China University of Geosciences, Beijing 100083,

10   People's Republic of China

11   [3] Frontiers Science Center for Deep-Time Digital Earth, China University of

12   Geosciences, Beijing 100083, People's Republic of China

13   [4] Institute of Geology, Chinese Academy of Geological Sciences, Beijing 100037,

14   People's Republic of China

15   [5] State Key Laboratory of Marine Geology, and School of Ocean and Earth

16   Science, Tongji University, Shanghai 200092, P. R. China

17   [6] College of Resource Environment and Earth Sciences, Yunnan University,

18   Kunming 650091, People's Republic of China

19

20   *Corresponding author at:

21   29 Xueyuan Road, Haidian District, Beijing 100083, China.

22   Tel: +8615011361152

23   E-mail: zhengyuanchuan@gmail.com **(Yuanchuan Zheng)**

24

25   29 Xueyuan Road, Haidian District, Beijing 100083, China.

26   Tel: +8618611688625

27   E-mail: xubo@outlook.com.cn (**Bo Xu**)

28

29   **Abstract**

30   Magmatic fluid degassing within shallow magma chambers underneath the ore

31   bodies is critical to the formation of porphyry Cu–Au deposits (PCDs). Yet, it

32   remains unclear that how the ways of fluid degassing influence on the

33   development of PCDs. Here, geochemical data of apatite, amphibole and

34   plagioclase from ore-forming and coeval barren porphyries have been analyzed in

35   Sanjiang metallogenic belt, China. The ore-forming porphyries normally exhibit

36   high and wide X_F/X_{Cl} (31.76–548.12) and X_F/X_{OH} (0.779–7.370) ratios of

37   apatites, which are evidently higher than those of the barren porphyries (X_F/X_{Cl} of

38   1.03–26.58; X_F/X_{OH} of 0.686–3.602). Combined with the continuous variation

39   features of Cl/OH ratios and H_2O contents of melts calculated by amphiboles, as

40   well as fluid migration models, we constrained the mechanisms of fluid degassing

41   within shallow magma chambers underneath PCDs. There are three different

42   ways of fluid degassing, while only fluid degassing via fluid channel stage can

43   migrate and focus the metal-rich fluids effectively, conducive to the development

44   of PCDs. The mechanisms of magmatic fluid degassing processes are further

45   controlled by the storage depths of magma chambers and initial H_2O contents of

46   the magmas revealed by the compositions of amphibole, plagioclase and

47   thermodynamic modelling. Magmas, with shallower storage depth and higher

48   initial H_2O content, are more likely to experience extensive and focused fluid

49   degassing, leading to the generation of PCDs. This study demonstrates the

50   potential utility of integrated mineral analyses, the thermodynamic modelling for

51   investigating the mechanisms of magmatic fluid degassing in porphyry systems,

52   as well as identifying prospective buried PCDs.

53

54   **Keywords:** porphyry deposit, magma degassing, magma chamber,

55   thermodynamic modelling, apatite, amphibole

56

57   **Introduction**

58   Porphyry Cu–Au deposits (PCDs), representing a typical type of magmatic–

59   hydrothermal deposit, currently provide ~75% and ~20% of the global demand

60   for Cu and Au, respectively (Sillitoe, 2010). Their ore bodies are typically around

61   the apical tips of small volume ($< $ ~5 km^3) pipe- or dyke-like porphyries at depths

62   of ~1–4 km. Such small porphyries could not be able to provide enough ore-

63   forming metals and fluids (enriched in H_2O, HCl, H_2S, SO_2 and other volatile

64   components) for the development of large PCDs. Thus, it is commonly believed

65   that the ore-forming metals and fluids are dominantly derived from a larger

66   magma chamber ($> $ ~100 km^3) underneath the porphyries at depths of ~4–10 km

67   (e.g., Richards., 2018). Consequently, the tonnages of PCDs could be closely

68   associated with the volumes of fluids ($> $ ~10 km^3) degassed from the shallow

69   magma chambers (e.g., Cline and Bodnar, 1991; Chelle-Michou et al., 2017;

70   Richards., 2018), while the processes of fluid degassing may also play critical

71   roles in the development of PCDs as shown by numerical simulations (Parmigiani

72   et al., 2016, 2017; Degruyter et al., 2019; Lamy-Chappuis et al., 2020). These

73   various processes that govern the transport and extraction of magmatic fluids, as

74   they leave their shallow magma chambers and reach the mineralization sites, are

75   difficult to be well constrained directly by geological samples, and remain a major

76   challenge to our understanding of magmatic–hydrothermal systems of PCDs.

77   Apatite and amphibole are common phases in ore-forming porphyries that can

78   incorporate Cl, F and OH in their structure and known to have a relatively high

79   crystal–melt partition coefficients of them. They have been used to elucidate the

80   behavior of magmatic fluids, owing to their ability to dynamically re-equilibrate

81   their volatiles contents in response to changes in melt compositions (Piccoli and

82   Candela, 2002; Humphreys et al., 2009). Therefore, the compositions of apatite

83   and amphibole might have great potential to provide well constrains on the

84   mechanisms of fluid degassing within the shallow magma chambers underneath

85   PCDs (e.g., Humphreys et al., 2009; Stock et al., 2016, 2018; Popa et al., 2021).

86   The comparisons of apatite and amphibole from ore-forming and barren magmas,

87   combined with correlative thermodynamic models, could be used to reveal the

88   significance of fluid degassing mechanisms in the development of PCDs and their

89   tonnages.

90   The Cenozoic Cu–Au metallogenic belt in Sanjiang region (Sanjiang metallogenic

91   belt), southwestern China, hosts numerous PCDs (Figure 1). They show broad

92   similarities in their formation ages, metal components and alteration patterns, and

93   are all related to adakite-like porphyries (Lu et al., 2013a, 2013b; Huang et al.,

94   2019), while the tonnages of these PCDs vary significantly. Meanwhile, there are

95   also some coeval adakite-like porphyries without mineralization (barren) in this

96   metallogenic belt. Collectively, these facts make the Sanjiang metallogenic belt an

97   excellent opportunity to examine how the mechanisms of fluid degassing in

98   shallow magma chambers control the formation of PCDs and provide the

99   guidance for PCDs mineral exploration.

100

Geological setting

102   The eastern Tibet Plateau, lying to Yangtze and Songpan–Ganze block, is built on

103   a tectonic collage of continental blocks resulted in progressive Triassic to

104   Cretaceous closures of the Paleo- and Neo-Tethyan Oceans (Figure 1). The

105   Cenozoic evolution of the eastern Tibet Plateau was largely controlled by Indian–

106   Asian collision, which was initiated at ca. 55 Ma (e.g., Najman et al., 2010; Deng

107   et al., 2014, 2021). The Indian–Asian continental collision caused crustal

108   thickening in Tibet (e.g., Najman et al., 2010), with continuing impingement of

109   the Indian plate on Asian causing the extrusion of elongated crustal blocks in

110   Sanjiang region, along the eastern Tibet Plateau (Figure 1; Tapponnier et al.,

111   1982).

112   During the Indian–Asian collision, the Eocene Sanjiang metallogenic belt formed

113   along Jinshajiang–Ailaoshan suture zone (JAS), which is largely composed of

114   relics of the Jinshajiang–Ailaoshan Paleo–Tethys oceanic plate (Figure 1; Deng et

115   al., 2014, 2021). The Sanjiang metallogenic belt clustered abundant Eocene

116   potassic felsic intrusions and potassic-ultrapotassic mafic volcanic rocks. There

117   are numerous PCDs along Sanjiang metallogenic belt, including two giant PCDs

118   of Yulong and Beiya as well as a series of large- to small-sized deposits (Lu et al.,

119   2013b; He et al., 2015; Hou et al., 2017; Huang et al., 2019; Xu et al., 2021;

120   Wang et al., 2022). The proven resources currently include >16 Mt Cu, >450 t

121   Au, ~6 Mt Mo (Lu et al., 2013b; Deng et al., 2014, 2021; He et al., 2015; Wang et

122   al., 2022). These PCDs were formed at ca. 34–43 Ma sharing similar metal

123   components and alteration patterns, and genetically related to adakite-like felsic

124   porphyries (ore-forming porphyries). Many Eocene adakite-like porphyries (32–

125   43 Ma) with no features of alteration and mineralization (barren porphyries) have

126   also been identified in this belt (Figure 1).

127   The ore-forming and barren adakite-like porphyries have similar outcrop area

128   (typically 0.5–1 km^2), dominated by pipe- or dyke-like intrusive bodies (Figure

129   1). The popular model proposes that these adakite-like porphyries were produced

130   by partial melting of sulfide-rich arc cumulates in the lower crust (e.g., Lu et al.,

131   2013; Hou et al., 2017; Huang et al., 2019; Shen et al., 2021). Additionally, some

132   scholars have also suggested that these adakite-like porphyries could be derived

133   from the fractionation of potassic mafic magmas derived from lithospheric mantle

134   (Jiang et al., 2006; Chang et al., 2023a). While there are potassic mafic rocks with

135   high La/Yb and Dy/Yb ratios similar to the felsic rocks, the scarcity of

136   corresponding high La/Yb and Dy/Yb samples in the intermediate-transitional

137   range undermines the credibility of the potassic mafic magmas fractionation

138   model (Supplementary Figure 1a, b). The elevated La/Yb and Dy/Yb ratios

139 observed in these adakite-like porphyries can be effectively explained by the

140 presence of residual garnet in the source (Davidson et al., 2007; Macpherson,

141 2008). Considering the similarities in geochemical signatures (e.g., adakite-like;

142 Supplementary Figure 1c, d) and isotopic compositions (ε_{Hf}(t): -9.1–8.5;

143 ($^{87}Sr/^{86}Sr)_i$: 0.7050–0.7097; ε_{Nd}(t): -11.2–1.43; Supplementary Figure 2), we are

144 inclined to believe that both ore-forming and barren adakite-like porphyries were

145 derived from partial melting of a juvenile lower crust resulting from previous

146 underplating of Neoproterozoic–Paleozoic arc magmas. The subduction of Indian

147 continent disturbed the asthenosphere of Asian continent, causing the upwelling

148 of mantle flow. The hot mantle flow rose through the mantle and widely emplaced

149 at crust–mantle boundary, resulting in large-scale partial melting of the lower

150 crust (e.g., Hou et al., 2021). The Jinshajiang–Ailaoshan suture zone, having

151 spatial correspondence with this hot mantle flow, dominates the emplacement of

152 potassic intrusions, forming the north-northwest trend 2000-km-long magmatic

153 belt (Figure 1; Hou et al., 2021; Deng et al., 2021).

154

155 **Sample description**

156 Combined with our previously data, systematic whole-rock and mineralogical

157 data from four ore-forming porphyries of PCDs, including two giant PCDs (Beiya

158 and Yulong) and two large PCDs (Machangqing and Yao'an), as well as six

159 barren porphyries (Shigu, Weishan, Ninglang, Yanyuan, Nangqian and

160 Mangkang) in the Sanjiang metallogenic belt have been analyzed in this paper

161 (Supplementary Table 1–7). The Yulong and Machangqing deposits contain Cu–

162   Mo mineralization (Yulong: ~6.5 Mt Cu, 0.4 Mt Mo; Machangqing: 0.3 Mt Cu,

163   0.1 Mt Mo) within the ~43 Ma and ~35 Ma porphyries. The Beiya and Yao'an

164   deposits exhibit Au mineralization (~320 t and ~10 t Au) related to the ~36 Ma

165   and ~33 Ma porphyries, respectively. The barren porphyries have been dated at

166   ~33 to 40 Ma, showing spatial and temporal correspondence with the ore-forming

167   porphyries.

168   The ore-forming and barren porphyries have similar mineral assemblages. The

169   phenocrysts contain plagioclase, K-feldspar, amphibole, biotite and quartz, and

170   some apatite micro-phenocrysts. Groundmass of these porphyries are composed

171   of plagioclase, K-feldspar and quartz with sizes mostly < 0.5 mm. The plagioclase

172   (0.2–4 mm) occurs as euhedral to subhedral laths (Figure 2a–g). Some plagioclase

173   grains preserve oscillatory zoning (Figure 2b, f). K-feldspar is mostly anhedral

174   with occasional cross-hatched (tartan) twinning. The biotite phenocrysts, which

175   are lath-shaped and range from euhedral to subhedral, exhibit yellowish to dark

176   brown pleochroism (Figure 2b, f). The quartz phenocrysts are irregular and

177   circular. Euhedral to subhedral amphibole phenocrysts are hexagon-shaped with

178   dark brown to green pleochroism, ranging from the 0.3 to 5 mm in size (Figure

179   2a–g). Some slightly fluid altered amphibole phenocrysts have bleached colors

180   corresponding to the patchy zoning observed in BSE images (Figure 2h), which

181   were excluded from the experiment. Apatites occur as inclusions within biotite

182   and K-feldspar phenocrysts apart from micro-phenocrysts (Figure 2j, 2k). Some

183   apatites exhibit bright bands along fractures and edges in cathodoluminescence

184   (CL) images (Figure 2l), indicating that these corresponding portions of apatite

185   have undergone late-stage hydrothermal alteration. We excluded these

186   hydrothermally altered apatites and took precautions during experiments to avoid

187   fluid or mineral inclusions and fractures in apatite to ensure that the tested apatites

188   are primarily magmatic origin (Supplementary Figure 3). Therefore, the selected

189   amphiboles and apatites are of primary magmatic origin (Figure 2i, 2l), and

190   capable of reflecting the corresponding magmatic processes and avoiding the

191   influence of late-stage hydrothermal alteration.

192

193   **Results**

194   Major element compositions of apatite, amphibole, and plagioclase from ore-

195   forming and barren porphyries in Sanjiang metallogenic belt were obtained using

196   an electron probe microanalyzer (EPMA). The results are presented in

197   Supplementary Table 1–3, including compiled data for Yao'an, Yulong, Nangqian

198   and Mangkang (e.g., Bi et al., 2009). For detailed information about the analytical

199   methods employed, please refer to the Supplementary materials.

200

201   **Amphibole compositions**

202   The analyzed amphibole phenocrysts in both ore-forming and barren porphyries

203   are unaltered, showing no bleached colors (Figure 2i). The quality of their

204   compositions was verified using AMFORM.xlsx (Ridolf et al., 2018). These

205   amphiboles are all calcic ($Ca_B > 1.5$) and can be further classified as actinolite,

206   magnesiohornblende, edenite and pargasite (Supplementary Figure 4a, b; Leake et

207   al., 1997). The amphibole phenocrysts in ore-forming porphyries demonstrate

208   variable contents of Na_2O (0.54–2.24 wt%), CaO (10.91–12.56 wt%), and Al_2O_3

209   (1.99–8.48 wt%). The amphibole phenocrysts in barren porphyries display

210   narrower ranges in Na_2O (1.45–3.01 wt%), CaO (10.91–11.94 wt%), and Al_2O_3

211   (6.63–12.12 wt%). The Al^{VI} contents of the amphiboles in ore-forming and barren

212   porphyries are 0.28–1.44 and 0.97–1.87, respectively. They exhibit similar ranges

213   of Cl contents (0.01–0.24 wt% and 0.02–0.19 wt%, respectively), with no

214   observed correlation between Cl and Mg# (Supplementary Table 2).

215

216   **Apatite compositions**

217   Apatites in the ore-forming and barren porphyries exhibit similar CaO, P_2O_5 and

218   SO_3 contents (52–59 wt%, 38–43 wt% and 0.03–1.44 wt%, respectively). Apatites

219   from ore-forming porphyries show much higher F (1.60–3.22 wt%) and lower Cl

220   (0.01–0.17 wt%) contents relative to those from barren porphyries (1.15–2.76

221   wt% F, 0.18–2.10 wt% Cl; Supplementary Table 1). These differences can be

222   translated to X_F, X_{Cl} and X_{OH} (Supplementary Figure 4c), which are the mole

223   fractions of F, Cl and OH, respectively.

224   Apatites from ore-forming porphyries tend to have a low and narrow range of

225   X_{Cl}/X_{OH} (0.003–0.148), high and wide extents of X_F/X_{Cl} (31.76–548.12) and

226   X_F/X_{OH} (0.779–7.370), showing a negative correlation between X_F and X_{Cl}, X_F

227   and X_{OH}, respectively. In contrast, the counterparts from barren porphyries have

228   high and wide X_{Cl}/X_{OH} ratios (0.073–1.041), low and narrow X_F/X_{Cl} (1.03–26.58)

229   and X_F/X_{OH} (0.686–3.602) ratios, with a negative correlation between X_{Cl} and

230   X_{OH} (Supplementary Table 1).

231

Feldspar compositions

233　Some plagioclase phenocrysts in ore-forming and barren porphyries are zoned.

234　The plagioclases we selected are those with no zone or the rims of the zoned

235　plagioclase phenocrysts, which could be in equilibrium with the residual evolved

236　melt. In ore-forming porphyries, the plagioclase phenocrysts range in composition

237　from albite to anorthoclase and oligoclase (An content = 0.6-34.0% and Or

238　content = 0.5-24.0%). Among them, the plagioclase phenocrysts in the Beiya ore-

239　forming porphyry have the lowest An content (0.6-2.8%). The compositions of

240　plagioclase phenocrysts in barren porphyries are comparable to those in ore-

241　forming porphyries, ranging from albite to oligoclase (An content = 2.4-30.7%

242　and Or content = 0.5-8.6%; Supplementary Figure 4d, Table 3).

243

Pressure, temperature and H_2O content estimates

245　The method of Ridolfi and Renzulli (2012) has been used to estimate the physical

246　(P, T) and compositional conditions (e.g., melt H_2O contents) at the time of

247　amphibole crystallization, based on amphibole compositions (Figure 3). This

248　method is recommended for studies aiming to discern the pre-eruptive conditions

249　and sub-volcanic processes such as magma storage for both calc-alkaline and

250　alkaline magmatic series (Ridolfi and Renzulli. 2012; Chelle-Michou et al., 2015;

251　Gorini et al., 2018), which is consistent with our samples. The amphibole

252　compositions in this study match those of the experimental amphiboles from

253　Ridolfi and Renzulli (2012). However, there are much debate surrounds the

254   accuracy of the calculated intensive variables (e.g. Walker et al., 2013; Erdmann

255   et al., 2014). Therefore, the methods of amphibole–plagioclase barometer and

256   feldspar–liquid hygrometer have been conducted to estimate the physical and

257   compositional conditions (especially P and melt H_2O contents) and verify the

258   credibility of these results (Anderson et al., 2008; Putirka, 2008). The results for

259   individual analyses can be found in Supplementary Table 2–4.

260   The pressures and temperatures calculated using the methods of Ridolfi and

261   Renzulli (2012) indicate that amphiboles from ore-forming porphyries record

262   lower crystallization temperatures (680–831 °C with uncertainties ± 23.5 °C) and

263   pressures (0.39–1.56 Kbar with uncertainties ± 11.5%), whereas amphiboles from

264   barren porphyries yield evidently higher temperature and pressure, except for

265   Shigu and Yanyuan barren porphyries (739–940 °C and 0.97–4.35 Kbar, with

266   uncertainties ± 23.5 °C and ± 11.5%, respectively; Figure 3; Supplementary Fig 5,

267   Table 2). We also calculated pressures using amphibole–plagioclase barometer

268   (Anderson et al., 2008), and obtained a range of pressures of 0.3–4.4 Kbar, which

269   is similar to the results estimated by the methods of Ridolfi and Renzulli (2012)

270   (Supplementary Table 4). The pressures calculated by these two methods of the

271   same porphyry are relatively consistent within this study (Supplementary Fig 5).

272   The new temperature-independent Al-in amphibole geobarometer of Médard and

273   Le Pennec (2022) returns similar pressure ranges for ore-forming and barren

274   porphyries and suggests a shallower storage depths for the ore-forming magmas.

275   Overall, the melt H_2O contents of ore-forming porphyries (4.2–6.3 wt% with

276   uncertainties ± 0.78 wt%) are slightly lower than those of barren porphyries (4.0–

277 8.1 wt% with uncertainties ± 0.78 wt%) by the methods of Ridolfi and Renzulli

278 (2012) (Figure 3; Supplementary Table 2). These results are also cosistent with

279 the melt H_2O contents calculated using feldspar–liquid hygrometer (Putirka,

280 2008), except for Beiya ore-forming porphyry (Supplementary Fig 6, Table 3).

281 The higher melt H_2O contents and temperatures calculated by plagioclase–liquid

282 in the Beiya porphyry may indicate the physical and compositional conditions for

283 the early crystallization of plagioclases, while the lower melt H_2O contents and

284 temperatures calculated by amphibole-only represent the conditions for the later

285 stage of magma evolution with the crystallization of amphiboles.

286

287   **Discussion**

288 **Modelling fractionation and fluid saturation**

289 According to the different pressures and temperatures estimated by amphiboles

290 from ore-forming and barren porphyries in Sanjiang metallogenic belt, the

291 evolutions of ore-forming and barren magmas have been modeled, over the

292 pressure of 1.2 Kbar (corresponding to ore-forming magmas) and 3 Kbar (for

293 barren magmas) by the Rhyolite-MELTS thermodynamic software (Gualda et al.,

294 2012). Because these magmas are attributed to the partial melting of a thickened

295 juvenile lower crust (Figure 3a; Supplementary Figure 1, 2; Lu et al., 2013a,

296 2013b; He et al., 2015; Hou et al., 2017; Huang et al., 2019; Wang et al., 2022),

297 the melt composition from partial melting experiments on a synthetic has been

298 used as the starting composition, which is close to the average lower continental

299 crust (Qian and Hermann, 2013; details in supplementary materials). Models were

13

300   run at the Ni-NiO buffer and with H_2O concentration of 4 wt% according to the

301   results calculated by amphibole compositions (Figure 3c, 4b), and were also the

302   best ones reproducing the stable phase assemblages observed in ore-forming and

303   barren porphyries (Figure 3a; Lu et al., 2013a, 2013b; He et al., 2015; Huang et

304   al., 2019; Wang et al., 2022).

305   The model results confirm the crystallization sequence: plagioclase (~980°C) ＋

306   amphibole (~920°C) ＋ quartz (~760°C) ＋ biotite (~750°C) ＋ apatite

307   (~730°C) ＋ K-feldspar (~740°C) at 1.2 Kbar, and plagioclase (~970°C) ＋

308   amphibole (~910°C) ＋ quartz (~800°C) ＋ biotite (~780°C) ＋ apatite

309   (~760°C) at 3 Kbar (Figure 5a). These match the observed phase assemblage in

310   ore-forming and barren porphyries. Apatites arrive on the liquidus as a late

311   phenocryst phase at both 1.2 and 3 Kbar, which is consistent with the high SiO_2

312   contents of the melt inclusions trapped by apatites in Yulong porphyries (Chang et

313   al., 2018). During fractionation, modeled melt MgO contents have similar

314   variation characteristics at 1.2 and 3 Kbar, which decrease when amphiboles

315   arrive on the liquidus (Figure 5a). Pressures greatly affect the behaviors of

316   dissolved H_2O contents. At 3 Kbar, modeled melt H_2O contents increase from the

317   beginning to 6.9 wt% before fluid saturation is achieved at ~50% crystallization,

318   whereas the fluid saturation is achieved much earlier at ~7% crystallization, with

319   melt H_2O contents around 4 wt% at 1.2 Kbar (Figure 3c; 5a). We have also

320   modeled sulfide saturation processes at 1.2 and 3 Kbar with initial S concentration

321   ~100 ppm (Smythe et al., 2017; Yao and Mungall, 2020). The saturation

322   conditions occur at 15% crystallization, and the modeled melt S contents decrease

14

323   with fractionation at both 1.2 and 3 Kbar. Pressures affect the modeled down-

324   temperature S evolution of the melt, that the melt S contents at 3 Kbar are a bit

325   higher than those at 1.2 Kbar after S saturation is achieved (Figure 5a).

326

327   **Fluid enrichment and degassing of ore-forming and barren magmas**

328   The crystallization pressures and temperatures calculated by amphibole from ore-

329   forming porphyries (pink trend; 0.39–1.56 Kbar; 680–831 °C) are lower than

330   those of barren porphyries (gray trend; 0.97–4.35 Kbar; 739–940 °C; Figure 4c

331   and d), suggesting that amphibole crystallization in ore-forming magmas (with

332   lower crystallization pressure conditions) is relatively later than that in barren

333   magmas. These are consistent with the thermodynamic modelling, that modeled

334   melt amphiboles arriving on the liquidus at 3 Kbar is earlier than that at 1.2 Kbar

335   (Figure 5a, 6a and c).

336   During crystallization process with H_2O-undersaturation, Cl/OH ratios of the

337   melts [$(Cl/OH)_m$] will decrease with increasing H_2O contents of melts, whereas

338    $(Cl/OH)_m$ and H_2O contents of melts could decrease together under H_2O-

339   saturation condition, according to the experimental exchange partition coefficient

340   of Cl/OH and Cl/H_2O ratios between fluid and melt (Sato et al., 2005). In the

341   Sanjiang metallogenic belt, though the $(Cl/OH)_m$ decrease through cooling

342   process within both ore-forming and barren magmas (Figure 4c), H_2O contents of

343   the ore-forming magmas first increase then decrease with the falling of $(Cl/OH)_m$

344   as revealed by amphiboles (Figure 4b). Conversely, H_2O contents of the barren

345   magmas are characterized by rising consistently, lacking of falling in H_2O

346   contents (Figure 4b). These features indicate that H_2O contents were enriched in

347   both of the ore-forming and barren magmas during the processes of amphibole

348   crystallization. However, H_2O saturation did not occur within the barren magmas,

349   while the ore-forming magmas experienced obvious H_2O saturation and degassing

350   processes. According to the thermodynamic modelling, amphibole crystallization

351   occurs at relatively early stages of magmatic evolution at both 1.2 and 3 Kbar (Fig

352   5a and 6a, c). Amphiboles could record the degassing processes of most of the

353   ore-forming magmas, while the degassing processes of some ore-forming magmas

354   (such as Yao'an) are not recorded by amphiboles, due to degassing processes

355   taking place after amphibole crystallization instead of there being no degassing

356   processes.

357   The obvious changes of F, Cl and OH contents of apatites indicate that they may

358   have higher potential to record degassing processes than amphiboles. That is, the

359   crystallization of apatites could be at later magmatic fractionation stage, which is

360   consistent with the results of thermodynamic modelling (Fig 5a and 6a–d;

361   Supplementary Figure 4c). Together with their application to elucidate the volatile

362   contents of melts (Stock et al., 2016; 2018), models can be built to estimate the

363   evolution of melt volatile composition, relying on apatite–melt exchange

364   coefficients (K) between F–OH and Cl–OH. Decreasing in X_F/X_{Cl} and X_F/X_{OH}

365   with the falling of X_{Cl}/X_{OH} ratios for apatites should represent H_2O-

366   undersaturated crystallization, when the order of crystal–melt partition

367   coefficients from high to low is F, Cl and H_2O. In contrast, H_2O-saturation

368   crystallization could be characterized by a strong decrease in apatite X_{Cl}/X_{OH},

369   with increasing X_F/X_{Cl} ratios (Figure 7a, b; Supplementary Figure 4c), owing to

370   much higher fluid–melt partition coefficients for Cl than those for F (Webster et

371   al., 2014). Therefore, as shown in Figure 7, a modal represents ~50%

372   crystallization at H_2O-undersaturated conditions starting from 4 wt% H_2O content

373   (according to our Rhyolite-MELTS thermodynamic modelling; the initial melt Cl

374   and F concentrations are set at 0.4 wt % and 0.15 %, based on the melt inclusion

375   data from the Sanjiang porphyries; Chang et al., 2023b), with crystal–melt

376   partition coefficients Dc/m F ≈ 0.99, Dc/m Cl ≈ 0.9 and Dc/m OH ≈ 0.01. During

377   the next differentiation under fluid-saturation conditions to 90% crystallization,

378   there are three trajectories of apatite compositional evolution, which show

379   gradually increasing X_F/X_{Cl} and X_F/X_{OH} ratios, indicating an increased degree of

380   fluid degassing. The fluid–melt partition coefficient has been set as Df/m F ≈ 0.9

381   and Df/m Cl ≈ 35, consistent with alkali melt–fluid halogen partitioning

382   experiments under magmatic conditions (Figure 7a, b; e.g., Borodulin et al., 2009;

383   Hsu et al., 2019).

384   Much higher X_F/X_{Cl} and lower X_{Cl}/X_{OH} ratios of apatites from ore-forming

385   porphyries suggest that the ore-forming magma crystallization were reached H_2O-

386   saturation and degassed extensive fluids during magmatic evolution (Figure 7a),

387   according to the apatite thermodynamic modelling. The H_2O contents calculated

388   by amphiboles from ore-forming porphyries are decreasing with increase of

389   apatite X_F/X_{Cl} ratios, which further restricts the fluid degassing of ore-forming

390   magmas (Figure 8b). The fluid saturation and degassing processes will be greatly

391   affected by the magma storage depths, because pressure is the most important

392   variable controlling the solubility of H_2O (e.g., Zhang et al., 1999; Ghiorso and

393   Gualda, 2015; Collins et al., 2020). The lower crystallization pressures (shallower

394   storage depths) of ore-forming magmas estimated by amphiboles indicate lower

395   H_2O solubility (easier to reach H_2O saturation) of them (Figure 3b), which also

396   concurs with the features of apatites, amphiboles and our Rhyolite-MELTS

397   modelling (Figure 4d; 5a).

398   Very low X_{Cl}/X_{OH} ratios of apatites from ore-forming porphyries are consistent

399   with sufficient isobaric H_2O-saturated fractionation at high Df/m Cl, where Cl is

400   efficiently extracted from the melt into the extensive fluid phase. The ratios of

401   X_F/X_{OH}, however, remain relatively low throughout this isobaric crystallization

402   process according to no H_2O loss (Figure 7b; Stock et al., 2018). Under the

403   following polybaric H_2O-saturation fractionation, which is a fast process with

404   violent H_2O loss (fluid degassing) from shallow magma chambers, the X_F/X_{OH}

405   ratios of apatites from ore-forming porphyries then curve towards higher values

406   immediately, resulting in wide ranges of X_F/X_{OH} ratios (Figure 7b; 8c, d; Stock et

407   al., 2018). Low X_{Cl}/X_{OH} and wide ranges of X_F/X_{OH} and X_F/X_{Cl} ratios of apatites

408   and low crystallization pressures estimated by amphiboles, therefore, suggest that

409   the ore-forming magmas experienced focused extensive fluid degassing with

410   shallower storage depths of magma chambers.

411   Being different from ore-forming magmas, the barren magmas, with higher

412   crystallization pressures estimated by amphiboles (Figure 3a, b; Supplementary

413   Figure 5), show fluid enrichment during crystallization process at H_2O-

414   undersaturated conditions (gradual increase of H_2O contents with relatively low

415   X_F/X_{Cl} ratios of apatites; Figure 3c; 4b; 7a; 8a, b), followed by fluid exsolution

416   under isobaric H_2O-saturation condition (with no H_2O loss; continuous reduction

417   of X_{Cl}/X_{OH} with low X_F/X_{Cl} and X_F/X_{OH} ratios of apatites; Figure 7b).

418

419   **Mechanisms of fluid degassing within shallow magma chambers**

420   The ore-forming and barren magmas experienced polybaric and isobaric H_2O-

421   saturation fractionation, respectively, according to the features of apatites and

422   amphiboles. However, the different ways of fluid degassing under H_2O-saturation

423   processes cannot be explained only by H_2O solubility of melts according to

424   pressure conditions of magma chambers. Here, three different ways of fluid

425   degassing have been identified in the Sanjiang metallgenic belt according to

426   thermodynamic modelling (Figure 5b) and apatite and amphibole compositions

427   (Figure 5c–e), (1) by discrete bubbles that roughly account for a few percentages

428   of the total amount of fluid degassing, which could be recorded by the early

429   crystallized amphiboles characterized by decreasing $(Cl/OH)_m$ with increasing

430   H_2O contents (Figure 5e); (2) by permeable degassing via fluid channel formation

431   that contributes to about 40–50% of the degassing, which could be indicated by

432   high X_F/X_{Cl} and X_F/X_{OH} ratios of apatites. The together decreasing $(Cl/OH)_m$ ratio

433   and H_2O contents calculated by some relatively late crystalline amphiboles can

434   also indicate this degassing stage (Figure 5c); and (3) degassing stops because

435   there is not enough fluid to form/stabilize connected pathways (bubbles remain

436   trapped in the mush), which could be recorded by the decreasing X_{Cl}/X_{OH} with

437   low X_F/X_{OH} ratios of apatites, representing isobaric fluid exsolution (Figure 5d).

438   The storage depth of magmas play an important role in controlling the

439   mechanisms of fluid degassing. At 3 Kbar (~10 km in depth), the simulated melts

440   can achieve H_2O-saturation at ~41% crystal volume fractions (~50%

441   crystallization), and finally exsolves a large amount of fluids (~3.5 wt%), but all

442   the exsolved fluids belongs to the third stage which remain trapped in the mush

443   with no degassing (green region in Figure 5b). At 1.2 Kbar (~4 km in depth),

444   however, H_2O-saturation is achieved at very early stage with ~6% crystal volume

445   fractions (~7 wt% crystallization), and the degassing occurs through stage 1 and

446   stage 2 and finally to stage 3. Up to 3.4 wt% H_2O can be exsolved controlled by

447   discrete bubbles and fluid channel degassing processes (Figure 5b; Parmigiani et

448   al., 2017). Conclusively, shallower storage depths (for ore-forming magmas)

449   would enhance the amount of fluid degassing before the trapped bubbles stage.

450   However, the Yanyuan and Shigu exhibit shallow storage depths, similar to those

451   of the ore-forming magmas, showing weak or no fluid degassing (Figure 7a, b;

452   8b, d), which could be caused by the melts with relatively lower initial H_2O

453   contents.

454   The initial H_2O content of magmas may also play an important factor affecting

455   the mechanisms of fluid degassing (Chiaradia, 2020; Rezeau and Jagoutz, 2020).

456   The same starting compositions with different initial H_2O contents (1–7 wt%) at

457   1.2 and 3 Kbar have been modeled (Figure 6a, c). The model results confirm that

458   the crystallization sequences are similar with different initial H_2O contents. The

459   crystallization of quartz and plagioclase will be delayed and the process of H_2O-

460   saturation will be enormously advanced, with higher initial H_2O contents (Figure

20

461   6a, c). At 1.2 Kbar, the initial H_2O content required for fluid degassing is greater

462   than 2 wt% (Figure 6a, b). ~85% fluid contents (3.4 wt%) could degas after ~90

463   wt% crystallization, when the initial H_2O content is 4 wt%. Almost all fluid

464   contents could undergo degassing process, if the initial H_2O content is 6 wt%

465   (Figure 6b). In contrast, at 3 Kbar, degassing process cannot occur unless the

466   initial H_2O content is more than 4 wt%. ~80% fluid contents (4.8 wt%) are able to

467   degas after ~87 wt% crystallization, if the initial H_2O content is 6 wt% (Figure

468   6d). These results imply that higher initial H_2O contents would increase the

469   amount of fluid degassing before the trapped bubbles stage.

470   Collectively, magmas with shallower storage depths and higher initial H_2O

471   contents can reach fluid saturation at earlier stages of crystallization processes and

472   undergo more intense fluid degassing through fluid channel stage. The deeper

473   storage depths and lower initial H_2O contents of magmas will block the degassing

474   processes via the trapped bubbles stage.

475

476   **Extensive focused fluid degassing driving the formation of porphyry deposits**

477   Cu, Au and S will effectively partition into the fluids due to similarly elevated

478   fluid/melt partition coefficients, which vary from 10 to 100, 2 to 100 and 20 to

479   280 (e.g., Zajacz et al., 2012; Audétat and Edmonds, 2020), respectively. Thus,

480   the effective fluid exsolution, which could carry a large amount of metals, plays a

481   primary role in the generation of PCDs. However, the barren porphyries in the

482   Sanjiang metallgenic belt (e.g., Weishan and Nangqian) also experienced H_2O

483   saturation processes with no porphyry mineralization, according to continuous

21

484 reduction of X_{Cl}/X_{OH} with low X_F/X_{Cl} and X_F/X_{OH} ratios of apatites (Figure 7a,

485 b). This is possibly caused by the lack of effective migration and focusing of the

486 exsolved fluids. The mechanisms of fluid degassing after exsolution within

487 magma chambers, therefore, may finally determine whether the porphyries have

488 the potential to form PCDs.

489 As shown above, the ore-forming magmas in the Sanjiang metallgenic belt

490 experienced focused extensive fluid degassing revealed by the features of apatites

491 and amphiboles. Shallower storage depths and higher initial H_2O contents of ore-

492 forming magmas made the magmatic fluid exsolution occur at very early stage. In

493 consequence, these earlier exsolved fluids should enriched in Cu, Au and S,

494 because less fractionation of sulfides could occur before earlier fluid saturation,

495 leading to that higher proportion of those ore-forming elements can be extracted

496 from the melt by these earlier exsolved fluids (Figure 5a; Smythe et al., 2017).

497 Most of these exsolved fluids could migrate efficiently through fluid channel

498 stage. Meanwhile, for the ore-forming magmas with shallow storage depths, it is

499 easy to form a stable tube ring network, a particularly efficient fluid transport

500 pathway (Oppenheimer et al., 2015; Edmonds and Woods, 2018; Lamy-Chappuis

501 et al., 2020). This stable tube ring network will establish within the magma

502 chambers close to H_2O saturation at the early stage of crystallization processes,

503 requiring relatively low initial H_2O contents (Figure 9b). Fluid exsolution of the

504 entire ore-forming magmas took place mainly through fluid channel stage and

505 laterally focused fluids flowed through the tube ring, and then focused degassed

506 from spatially stable small region in the roof of the magma chambers, which is

507   consistent with wide ranges of X_F/X_{OH} and low X_{Cl}/X_{OH} ratios of apatites (Figure

508   9b). The metal sulfides were settled in relatively small volume rocks accordingly

509   (porphyry mineralization) at the end.

510   Conversely, the barren magmas with deep storage depths could also undergo fluid

511   saturation (Figure 9c, d), which occurred at late stage of crystallization processes.

512   Most of the exsolved fluids would be trapped within the magma chambers at

513   trapped bubbles stage. Even if the storage depths of the barren magmas from

514   Yanyuan and Shigu are shallow, their low initial H_2O contents (less than 2 wt%,

515   according to our thermodynamic modelling with different initial H_2O contents;

516   Figure 6b) blocked the migration of exsolved fluids (mainly at trapped bubbles

517   stage; Figure 6b; 9a). It is also difficult to form an integral tube ring network for

518   the barren magmas with deep storage depths and/or low initial H_2O contents

519   (Figure 9a, c, d). Fluid degassing within the barren magma chambers is weaker,

520   more radial and diffusive, recorded by slight increase in X_F/X_{OH} with low

521   X_{Cl}/X_{OH} ratios of apatites (as in Shigu and Weishan barren magma chambers; Fig

522   9a, d), or there is no degassing at all, revealed by declining of X_{Cl}/X_{OH} with low

523   X_F/X_{OH} ratios of apatites (Figure 9c). Without or with limited magmatic fluid

524   degassing, the ore-forming elements cannot be effectively focused and migrated

525   from the magma chambers, resulting in no porphyry mineralization.

526   Magmatic fluid degassing processes bridge the magmatic and hydrothermal

527   systems of PCDs, during magma ascent and storage in the upper crust with

528   cooling and crystallization at a fixed pressure (e.g., Parmigiani et al., 2016, 2017).

529   In the Sanjiang metallgenic belt, only magmas with shallow storage depths

530   (commonly less than ~5 km) and relatively high initial H_2O contents (at least ~2

531   wt%) allow effective migration, focusing and degassing processes of metal-rich

532   exsolved fluids, which are pre-requisites to the precipitation of metal sulphides

533   within a relatively small volume of rock, the final step in the formation of PCDs.

534

535   **Implications for exploration**

536   The mineral geochemical data and thermodynamic modelling presented here

537   allow us to shed light on the control of the mechanisms of fluid degassing within

538   shallow magma chambers on the formation of PCDs. This multiscale approach

539   reveals that only if H_2O-saturation is achieved at the early stage of magmatic

540   evolution, the exsolved fluids carrying ore-forming elements can migrate

541   efficiently through fluid channel stage, focus through the tube ring and degas

542   from spatially small region in the roof of shallow magma chambers. Magmas with

543   shallower storage depths and higher initial H_2O contents can reach fluid saturation

544   at earlier stages of crystallization processes and allow more substantial focused

545   degassing, leading to significant ore-forming elements focusing and the formation

546   of PCDs. Conversely, deeper storage depths and lower initial H_2O contents can be

547   more prone to a late-stage fluid exsolution where fluids remain trapped in the

548   mush with no degassing.

549   The combination of apatite, amphibole and plagioclase analyses and

550   thermodynamic modelling represents a robust approach for assessing the

551   mechanisms of fluid degassing in the upper crust, which could reveal the

552   transformation processes from magmatic systems to hydrothermal systems. This

24

553   approach can significantly advance our understanding of the ore-forming

554   processes of PCDs, which can be an effective exploration tool to reveal the

555   degassing processes of magmas and the optimal storage depths conducive to

556   porphyry mineralization, and thus to identify prospective buried PCDs.

557

558   **Acknowledgments**

571

572   **References cited**

573   Anderson, J.L., Barth, A.P., Wooden, J.L., and Mazdab, F. (2008). Thermometers

574   and thermobarometers in granitic systems. Reviews in mineralogy and

575   geochemistry, 69(1), 121–142.

576   Annen, C., Blundy, J.D., and Sparks, R.S.J. (2006). The genesis of intermediate

577   and silicic magmas in deep crustal hot zones. Journal of Petrology, 47(3), 505–

578   539.

579   Audétat, A., and Edmonds, M. (2020). Magmatic–hydrothermal fluids. Elements:

580   An International Magazine of Mineralogy, Geochemistry, and Petrology, 16(6),

581   401–406.

582   Bi, X.W., Hu, R.Z., Hanley, J.J., Mungall, J.E., Peng, J.T., Shang, L.B., Wu, K.X.,

583   Suang, Y., L, H.L., and Hu, X.Y. (2009). Crystallisation conditions (t, p, fO_2)

584   from mineral chemistry of Cu- and Au-mineralised alkaline intrusions in the Red

585   River–Jinshajiang alkaline igneous belt, western Yunnan province, china.

586   Mineralogy & Petrology, 96(1–2), 43.

587   Borodulin, G.P., Chevychelov, V.Y., and Zaraysky, G.P. (2009). Experimental

588   study of partitioning of tantalum, niobium, manganese, and fluorine between

589   aqueous fluoride fluid and granitic and alkaline melts. Doklady Earth Sciences,

590   427, 868–873.

591   Chang, J. and Audétat, A. (2023a) Post-subduction porphyry Cu magmas in the

592   Sanjiang region of southwestern China formed by fractionation of lithospheric

593   mantle–derived mafic magmas. Geology, 51(1), 64–68.

594   Chang, J. and Audétat, A. (2023b). Experimental Equilibrium and Fractional

595   Crystallization of a H_2O, CO_2, Cl, and S-bearing Potassic Mafic Magma at 1.0

596   GPa, with Implications for the Origin of Porphyry Cu (Au, Mo)-forming Potassic

597   Magmas. Journal of Petrology, egad034.

598   Chiaradia, M. (2020). Gold endowments of porphyry deposits controlled by

599 precipitation efficiency. Nature Communications, 11(1), 248.

600 Chang, J., Li, J.W., and Audétat, A. (2018). Formation and evolution of

601 multistage magmatic–hydrothermal fluids at the Yulong porphyry Cu–Mo

602 deposit, eastern Tibet: Insights from LA–ICP–MS analysis of fluid inclusions.

603 Geochimica et Cosmochimica Acta, 232, 181–205.

604 Chelle-Michou, C., Chiaradia, M., Beguelin, P., and Ulianov, A. (2015).

605 Petrological evolution of the magmatic suite associated with the Coroccohuayco

606 Cu (–Au–Fe) Porphyry–skarn deposit, Peru. Journal of Petrology, 56(9), 1829–

607 1862.

608 Chelle-Michou, C., Rottier, B., Caricchi, L., and Simpson, G. (2017). Tempo of

609 magma degassing and the genesis of porphyry copper deposits. Scientific reports,

610 7(1), 1–12.

611 Cline, J.S., and Bodnar, R.J. 1991. Can economic porphyry copper mineralization

612 be generated by a typical calc-alkaline melt?. Journal of Geophysical Research:

613 Solid Earth, 96(B5), 8113-8126.

614 Collins, W.J., Murphy, J.B., Johnson, T.E., and Huang, H.Q. (2020). Critical role

615 of water in the formation of continental crust. Nature Geoscience, 13(5), 331–338.

616 Degruyter, W., Parmigiani, A., Huber, C., and Bachmann, O. (2019). How do

617 volatiles escape their shallow magmatic hearth? Philosophical Transactions.

618 Series A, Mathematical, Physical, and Engineering Sciences, 377(2139),

619 20180017.

620 Davidson, J., Turner, S., Handley, H., Macpherson, C., Dosseto, A. (2007).

621 Amphibole "sponge" in arc crust?. Geology, 35(9), 787–790.

622   Deng, J., Wang, Q.F., Li, G.J., and Santosh, M. (2014). Cenozoic tectono-

623   magmatic and metallogenic processes in the Sanjiang region, southwestern China.

624   Earth-Science Reviews, 138, 268–299.

625   Deng, J., Wang, Q.F., Gao, L., He, W.Y., Yang, Z.Y., Zhang, S.H., Chang, L.J.,

626   Li, G.J., Sun, X., and Zhou, D.Q. (2021). Differential crustal rotation and its

627   control on giant ore clusters along the eastern margin of Tibet. Geology, 49(4),

628   428–432.

629   Edmonds, M., and Woods, A.W. (2018). Exsolved volatiles in magma reservoirs.

630   Journal of Volcanology and Geothermal Research, 368, 13–30.

631   Erdmann, S., Martel, C., Pichavant, M., and Kushnir, A. (2014). Amphibole as an

632   archivist of magmatic crystallization conditions: problems, potential, and

633   implications for inferring magma storage prior to the paroxysmal 2010 eruption of

634   Mount Merapi, Indonesia. Contributions to Mineralogy and Petrology, 167, 1–23.

635   Ghiorso, M.S., and Gualda, G.A. (2015). An H_2O–CO_2 mixed fluid saturation

636   model compatible with rhyolite-MELTS. Contributions to Mineralogy and

637   Petrology, 169(6), 1–30.

638   Gorini, A., Ridolfi, F., Piscaglia, F., Taussi, M., and Renzulli, A. (2018).

639   Application and reliability of calcic amphibole thermobarometry as inferred from

640   calc-alkaline products of active geothermal areas in the Andes. Journal of

641   Volcanology and geothermal Research, 358, 58–76.

642   Gualda, G.A.R., Ghiorso, M.S., Lemons, R.V., and Carley, T.L. (2012). Rhyolite-

643   MELTS: a modified calibration of MELTS optimized for silica-rich, fluid-bearing

644   magmatic systems. Journal of Petrology, 53(5), 875–890.

645   He, W.Y., Mo, X.X., He, Z.H., White, N.C., Chen, J.B., Yang, K.H., Wang, R.,

646   Yu, X.H., Dong, G.C., and Huang, X.F. (2015). The geology and mineralogy of

647   the Beiya skarn gold depposit in Yunnan, southwest China. Economic Geology,

648   110, 1625–1641.

649   Hou, Z.Q., Zhou, Y., Wang, R., Zheng, Y.C., He, W.Y., Zhao, M., Evans, N.J.,

650   and Weinberg, R.F. (2017). Recycling of metal-fertilized lower continental crust:

651   Origin of non-arc Au-rich porphyry deposits at cratonic edges. Geology, 45(6),

652   563–566.

653   Hou, Z.Q., Xu, B., Zheng, Y.C., Zheng, H.W., and Zhang, H.R. (2021) Mantle

654   flow: The deep mechanism of large-scale growth in Tibetan Plateau. Chinese

655   Science Bulletin, 66, 2671–2690 (in Chinese with English abstract).

656   Hsu, Y.J., Zajacz, Z., Ulmer, P., and Heinrich, C.A. (2019). Chlorine partitioning

657   between granitic melt and H_2O–CO_2–NaCl fluids in the Earth's upper crust and

658   implications for magmatic–hydrothermal ore genesis. Geochimica et

659   Cosmochimica Acta, 261, 171–190.

660   Huang, M.L., Bi, X.W., Hu, R.Z., Gao, J.F., Xu, L.L., Zhu, J.J., and Shang, L.B.

661   (2019). Geochemistry, in-situ Sr–Nd–Hf–O isotopes, and mineralogical

662   constraints on origin and magmatic-hydrothermal evolution of the Yulong

663   porphyry Cu-Mo deposit, Eastern Tibet. Gondwana Research, 76, 98–114.

664   Humphreys, M.C.S., Edmonds, M., Christopher, T., and Hards, V. (2009).

665   Chlorine variations in the magma of Soufrière Hills Volcano, Montserrat: Insights

666   from Cl in hornblende and melt inclusions. Geochimica et Cosmochimica Acta,

667   73(19), 5693–5708.

668   Iacono-Marziano, G., Morizet, Y., Le Trong, E., and Gaillard, F. (2012). New

669   experimental data and semi-empirical parameterization of H_2O–CO_2 solubility in

670   mafic melts. Geochimica et Cosmochimica Acta, 97, 1–23.

671   Jiang, Y.H., Jiang, S.Y., Ling, H.F., Dai, B.Z. (2006). Low-degree melting of a

672   metasomatized lithospheric mantle for the origin of Cenozoic Yulong

673   monzogranite-porphyry, east Tibet: geochemical and Sr–Nd–Pb–Hf isotopic

674   constraints. Earth and Planetary Science Letters, 241(3-4), 617–633.

675   Lamy-Chappuis, B., Heinrich, C.A., Driesner, T., and Weis, P. (2020).

676   Mechanisms and patterns of magmatic fluid transport in cooling hydrous

677   intrusions. Earth and Planetary Science Letters, 535, 116111.

678   Leake, B.E., Woolley, A.R., Arps, C.E.S., Birch,W.D., Charles Gilbert, M., Grice,

679   J.D., Hawthorne, F.C., Kato, A., Kisch, H.J., Krivovichev, V.G., Linthout, K.,

680   Laird, J., Mandarino, J.A., Maresch,W.V., Nickel, E.H., Rock, N.M.S.,

681   Schumacher, J.C., Simith, D.C., Stephenson, N.C.N., Ungaretti, L., Whittaker,

682   E.J.W., and Guo, Y.Z. (1997). Nomenclature of amphiboles; report of the

683   Subcommittee on Amphiboles of the International Mineralogical Association

684   Commission on new minerals and mineral names. The Canadian Mineralogist,

685   35(1), 219–246.

686   Lu, Y.J., Kerrich, R., Mccuaig, T.C., Li, Z.X., Hart, C.J., Cawood, P.A., Hou,

687   Z.Q., Bagas, L., Cliff, J., Belousova, E.A., and Tang, S.H. (2013a). Geochemical,

688   Sr–Nd–Pb, and zircon Hf–O isotopic compositions of Eocene–Oligocene

689   shoshonitic and potassic adakite-like felsic intrusions in western Yunnan, SW

690   China: petrogenesis and tectonic implications. Journal of Petrology, 54(7), 1309–

691   1348.

692   Lu, Y.J., Kerrich, R., Kemp, A.I., McCuaig, T.C., Hou, Z.Q., Hart, C.J., Li, Z.X.,

693   Cawood, P.A., Bagas, L., Yang, Z.M., Cliff, J., Belousova, E.A., Jourdan, F., and

694   Evans, N.J. (2013b). Intracontinental Eocene–Oligocene porphyry Cu mineral

695   systems of Yunnan, western Yangtze Craton, China: compositional

696   characteristics, sources, and implications for continental collision metallogeny.

697   Economic Geology, 108(7), 1541–1576.

698   Macpherson, C.G. (2008). Lithosphere erosion and crustal growth in subduction

699   zones: Insights from initiation of the nascent East Philippine Arc. Geology, 36(4),

700   311–314.

701   Najman, Y., Appel, E., Boudagher-Fadel, M., Bown, P., Carter, A., Garzanti, E.,

702   Godin, L., Han, J.T., Liebke, U., Oliver, G., Parrish, R., and Vezzoli, G. (2010).

703   Timing of India–Asia collision: Geological, biostratigraphic, and palaeomagnetic

704   constraints. Journal of Geophysical Research: Solid Earth, 115, B12.

705   Newman, S., and Lowenstern, J.B. (2002). VolatileCalc: a silicate melt–H_2O–CO_2

706   solution model written in Visual Basic for excel. Computers & Geosciences,

707   28(5), 597–604.

708   Oppenheimer, J., Rust, A.C., Cashman, K.V., and Sandnes, B. (2015). Gas

709   migration regimes and outgassing in particle-rich suspensions. Frontiers in

710   Physics, 3, 60.

711   Papale, P., Moretti, R., and Barbato, D. (2006). The compositional dependence of

712   the saturation surface of $H_2O + CO_2$ fluids in silicate melts. Chemical Geology,

713   229(1–3), 78–95.

714   Parmigiani, A., Faroughi, S., Huber, C., Bachmann, O., and Su, Y. (2016). Bubble

715   accumulation and its role in the evolution of magma reservoirs in the upper crust.

716   Nature, 532 (7600), 492–495.

717   Parmigiani, A., Degruyter, W., Leclaire, S., Huber, C., and Bachmann, O. (2017).

718   The mechanics of shallow magma reservoir outgassing. Geochemistry,

719   Geophysics, Geosystems, 18(8), 2887–2905.

720   Piccoli, P.M., and Candela, P.A. (2002). Apatite in igneous systems. Reviews in

721   Mineralogy and Geochemistry, 48(1), 255–292.

722   Popa, R.G., Tollan, P., Bachmann, O., Schenker, V., Ellis, B., and Allaz, J. M.

723   (2021). Water exsolution in the magma chamber favors effusive eruptions:

724   Application of Cl–F partitioning behavior at the Nisyros–Yali volcanic area.

725   Chemical Geology, 570, 120170.

726   Putirka, K.D. (2008). Thermometers and barometers for volcanic systems.

727   Reviews in mineralogy and geochemistry, 69(1), 61–120.

728   Putirka, K.D. (2016). Amphibole thermometers and barometers for igneous

729   systems and some implications for eruption mechanisms of felsic magmas at arc

730   volcanoes. American Mineralogist, 101(4), 841–858.

731   Qian, Q., and Hermann, J. (2013). Partial melting of lower crust at 10–15 kbar:

732   constraints on adakite and TTG formation. Contributions to Mineralogy and

733   Petrology, 165(6), 1195–1224.

734   Rezeau, H., and Jagoutz, O. (2020). The importance of H2O in arc magmas for

735   the formation of porphyry Cu deposits. Ore Geology Reviews, 126, 103744.

736   Richards, J.P. (2018). A shake-up in the porphyry world?. Economic Geology,

737   113(6), 1225–1233.

738   Ridolfi, F., and Renzulli, A. (2012). Calcic amphiboles in calc-alkaline and

739   alkaline magmas: thermobarometric and chemometric empirical equations valid

740   up to 1,130 °C and 2.2 GPa. Contributions to Mineralogy and Petrology, 163(5),

741   877–895.

742   Ridolfi, F., Zanetti, A., Renzulli, A., Perugini, D., Holtz, F., Oberti, R. (2018).

743   AMFORM, a new mass-based model for the calculation of the unit formula of

744   amphiboles from electron microprobe analyses. American Mineralogist: Journal

745   of Earth and Planetary Materials, 103(7), 1112–1125.

746   Sato, H., Holtz, F., Behrens, H., Botcharnikov, R., and Nakada, S. (2005).

747   Experimental petrology of the 1991–1995 Unzen dacite, Japan. Part II: Cl/OH

748   partitioning between hornblende and melt and its implications for the origin of

749   oscillatory zoning of hornblende phenocrysts. Journal of Petrology, 46(2), 339–

750   354.

751   Shen, Y., Zheng, Y.C., Hou, Z.Q., Zhang, A.P., Huizenga, J.M., Wang, Z.X., and

752   Wang, L. (2021). Petrology of the Machangqing complex in Southeastern Tibet:

753   implications for the genesis of potassium-rich adakite-like intrusions in collisional

754   zones. Journal of Petrology, 62(11), egab066.

755   Sillitoe, R.H. (2010). Porphyry copper systems. Economic geology, 105, 3–41.

756   Smythe, D.J., Wood, B.J., and Kiseeva, E.S. (2017). The S content of silicate

757   melts at sulfide saturation: new experiments and a model incorporating the effects

758   of sulfide composition. American Mineralogist, 102(4), 795–803.

759   Stock, M.J., Humphreys, M.C., Smith, V.C., Isaia, R., and Pyle, D.M. (2016).

760   Late-stage volatile saturation as a potential trigger for explosive volcanic

761   eruptions. Nature Geoscience, 9, 249–254.

762   Médard, E., and Le Pennec, J.L. (2022). Petrologic imaging of the magma

763   reservoirs that feed large silicic eruptions. Lithos, 428, 106812.

764   Stock, M.J., Humphreys, M.C., Smith, V.C., Isaia, R., Brooker, R.A., and Pyle,

765   D.M. (2018). Tracking volatile behaviour in sub-volcanic plumbing systems using

766   apatite and glass: insights into pre-eruptive processes at Campi Flegrei, Italy.

767   Journal of Petrology, 59(12), 2463–2492.

768   Tapponnier, P., Peltzer, G.L.D.A.Y., Le Dain, A.Y., Armijo, R., and Cobbold, P.

769   (1982). Propagating extrusion tectonics in Asia: New insights from simple

770   experiments with plasticine. Geology, 10, 611–616.

771   Walker, B.A., Klemetti, E.W., Grunder, A.L., Dilles, J.H., Tepley, F.J., and Giles,

772   D. (2013). Crystal reaming during the assembly, maturation, and waning of an

773   eleven-million-year crustal magma cycle: thermobarometry of the Aucanquilcha

774   Volcanic Cluster. Contributions to Mineralogy and Petrology, 165, 663–682.

775   Wang, Z.X., Zheng, Y.C., Xu, B., Hou, Z.Q., Zhang, A.P., Shen, Y., Ma, R., Wu,

776   C.D., and Xu, P.Y. (2022). Hydrous Juvenile Lower Crust at the Western Yangtze

777   Craton Margin as the Main Source of the Beiya Porphyry–skarn Au Deposit. Acta

778   Geologica Sinica–English Edition, 96(3), 972–992.

779   Webster, J.D., Goldoff, B., Sintoni, M.F., Shimizu, N., and De Vivo, B. (2014).

780   C–O–H–Cl–S–F volatile solubilities, partitioning, and mixing in phonolitic–

781   trachytic melts and aqueous–carbonic vapor ± saline liquid at 200 MPa. Journal of

782   Petrology, 55, 2217–2248.

783   Xu, B., Hou, Z.Q., Griffin, W.L., Zheng, Y.C., Wang, T., Guo, Z., Hou, J.,

784   Santosh, M., and O'Reilly, S.Y. (2021). Cenozoic lithospheric architecture and

785   metallogenesis in Southeastern Tibet. Earth-Science Reviews, 214, 103472.

786   Yao, Z., and Mungall, J.E. (2020). Flotation mechanism of sulphide melt on

787   vapour bubbles in partially molten magmatic systems. Earth and Planetary

788   Science Letters, 542, 116298.

789   Zajacz, Z., Candela, P.A., Piccoli, P.M., and Sanchez-Valle, C. (2012). The

790   partitioning of sulfur and chlorine between andesite melts and magmatic volatiles

791   and the exchange coefficients of major cations. Geochimica et Cosmochimica

792   Acta, 89, 81–101.

793   Zhang, Y., 1999. H_2O in rhyolitic glasses and melts: measurement, speciation,

794   solubility, and diffusion. Reviews of Geophysics, 37(4): 493–516.

795
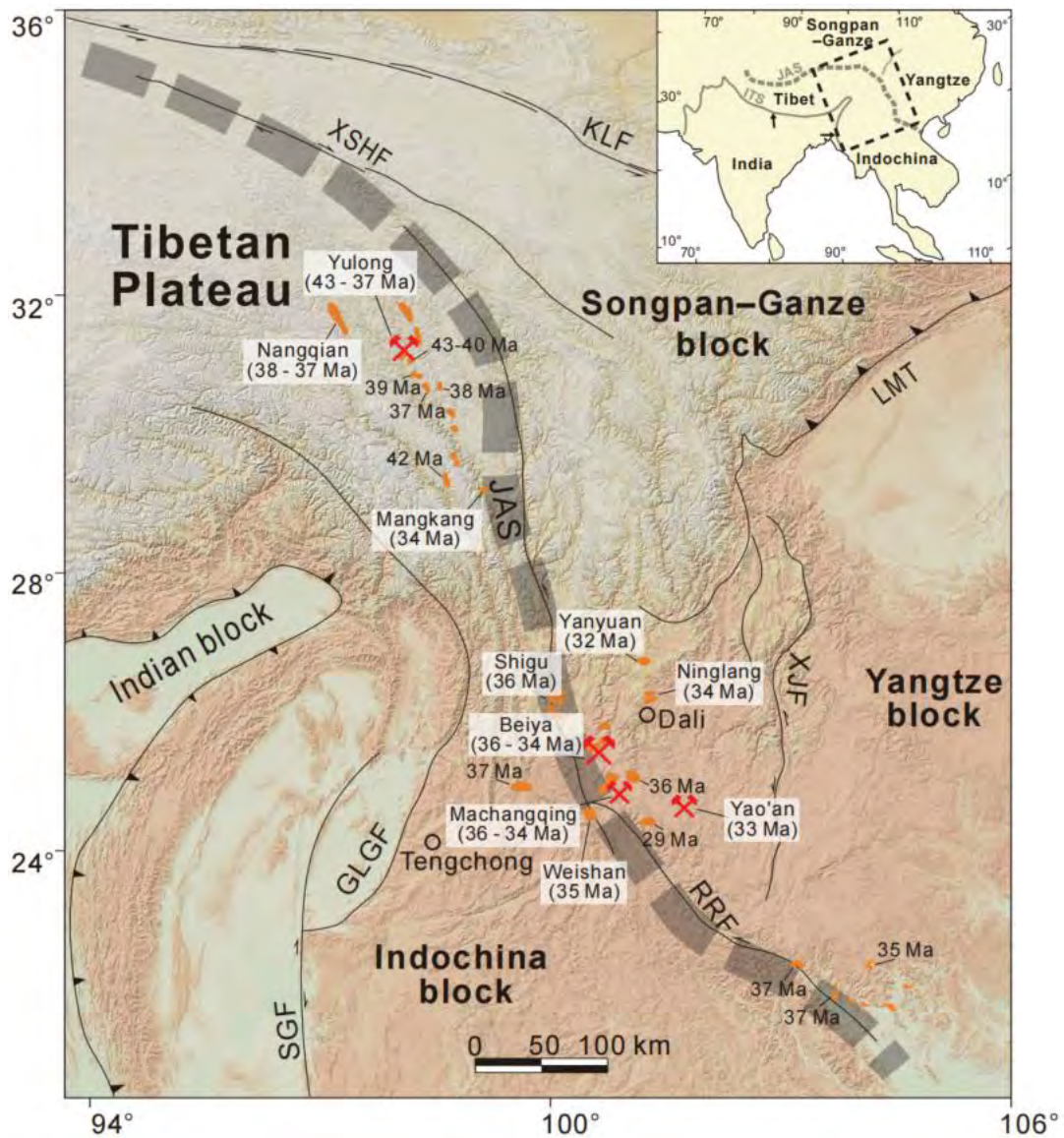
Figure 1. Topographic-geological map of the eastern Indian–Asian collisional

zone (Xu et al., 2021). The thick gray dotted line is Jinshajiang–Ailaoshan suture

(JAS), and the gray continuous line is Indus–Tsangpo suture. The PCDs are

shown as red hammers, including the giant Yulong (age of 43–37 Ma), giant

Beiya (age of 36–34 Ma), medium Machangqing (age of 36–34 Ma) and medium

Yao'an (age of 33 Ma; Lu et al., 2013b; Huang et al., 2019). The barren

porphyries along JAS are shown in orange. The black lines represent Cenozoic

804   faults (SGF: Sagaing fault; GLGF: Gaoligong fault; XSHF: Xianshuihe fault;

805   RRF: Red-River fault; XJF: Xiaojiang faults; LMT: Longenshan thrust fault;

806   KLF: Kunlun fault).

807

808
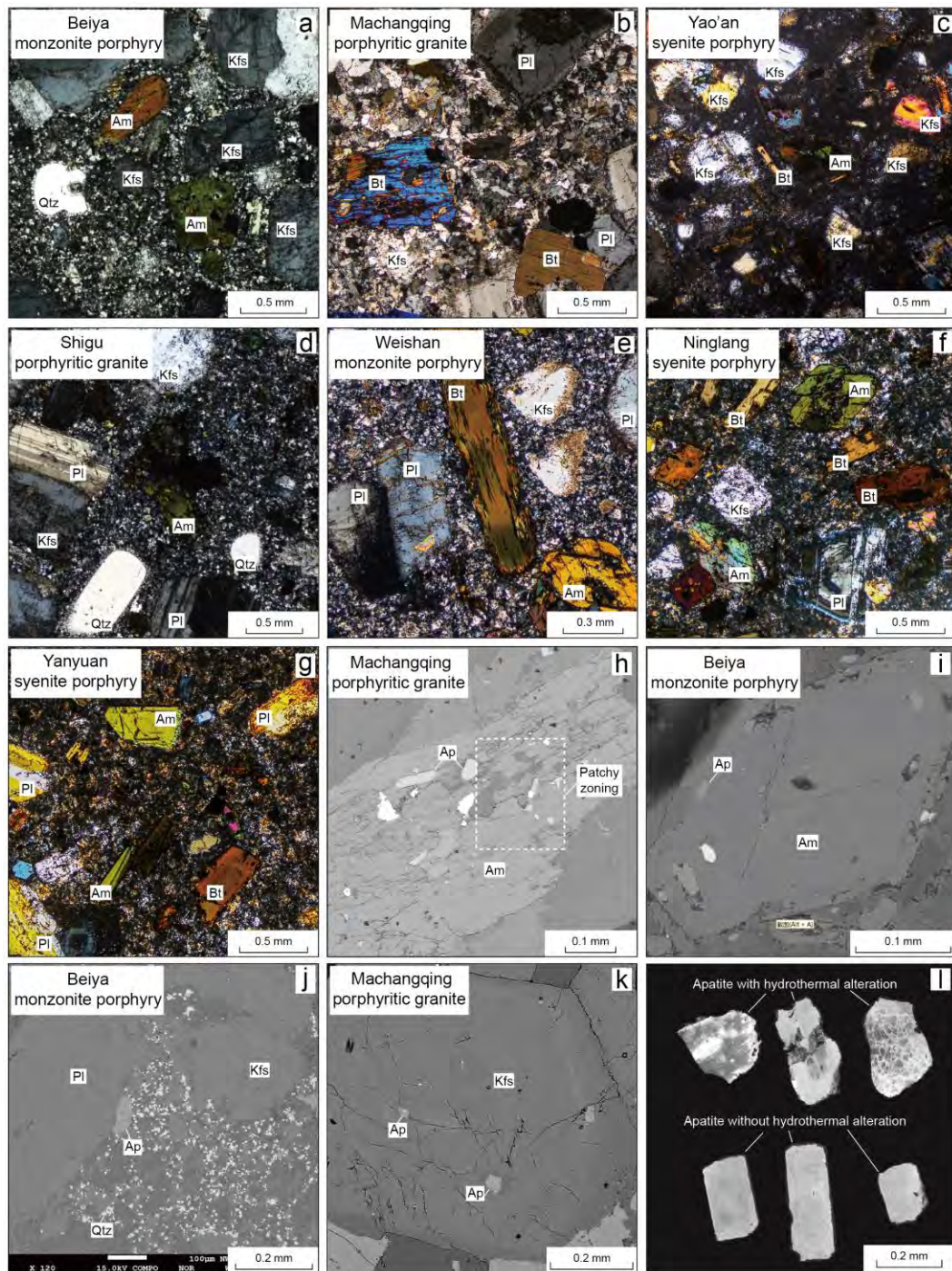
Figure 2. a–g, Photomicrographs of ore-forming and barren adakite-like

porphyries in Sanjiang metallogenic belt. **h and i,** Backscattered-electron (BSE)

images showing altered amphibole phenocryst (**h**) and amphibole phenocryst with

no hydrothermal alteration (**i**). **j and k,** Backscattered-electron (BSE) images

813 showing apatite microphenocryst (**j**) and apatite inclusions (**k**). **l,**

814 Cathodoluminescence (CL) images of apatite from ore-forming and barren

815 adakite-like porphyries. Qtz, quartz; Kfs, K-feldspar; Pl, plagioclase; Bt, biotite;

816 Am, amphibole; Ap, apatite.

817

818
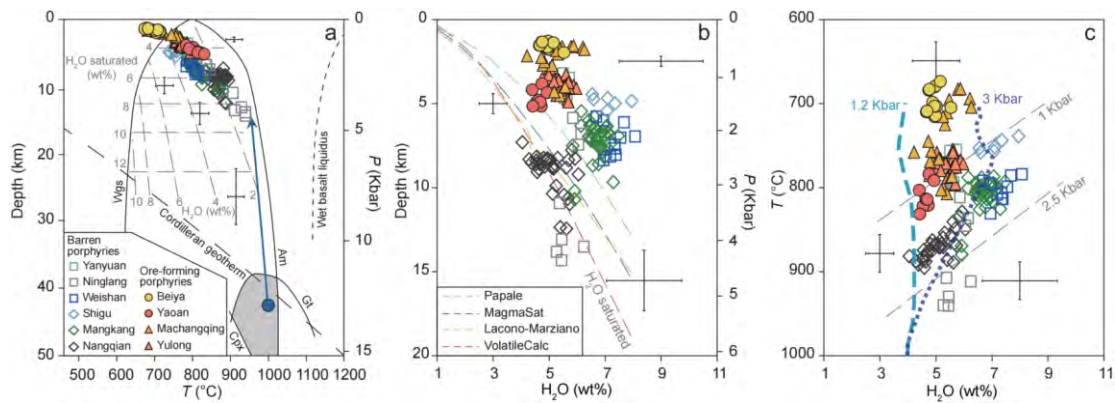
Figure 3. a, The calculated P–T conditions for the adakite-like porphyries in

Sanjiang metallogenic belt. Cross bars indicate the P–T uncertainties (Ridolfi and

Renzulli, 2012). Liquidus and near liquidus fields for amphibole, garnet,

clinopyroxene are delineated with black solid lines, labelled on their unstable side

(Annen et al., 2006). The field of residual garnet amphibolite is shaded. The blue

P–T path for partial melting of thickened juvenile lower crust (residual garnet

amphibolite; Annen et al., 2006), according to regional tectonic background of

Sanjiang region (Hou et al., 2017). The wet granite solidus line and wet basalt

liquidus line are delineated with black solid line and dashed line, respectively

(Collins et al., 2020). The steep grey dashed lines are undersaturated liquidus

(with wt% H_2O labelled) and the subhorizontal dashed lines are H_2O solubility

limits (also labelled as H_2O saturated; Gualda et al., 2012; Collins et al., 2020).

The cordilleran geotherm is also shown. Abbreviations: Cpx, clinopyroxene; Am,

amphibole; Gt, garnet; Wgs, wet granite solidus. **b,** The calculated magma depth

vs. magmatic H_2O content for the adakite-like porphyries in Sanjiang

metallogenic belt. Cross bars indicate the P–H_2O uncertainties (Ridolfi and

Renzulli, 2012). The colored dashed line show the H_2O solubility curves from

different methods (Newman and Lowenstern, 2002; Papale et al., 2006; Iacono-

40

837   Marziano et al., 2012; Ghiorso and Gualda, 2015). **c,** The calculated T–H_2O

838   conditions for the adakite-like porphyries in Sanjiang metallogenic belt. Cross

839   bars indicate the T–H_2O uncertainties (Ridolfi and Renzulli, 2012). The thick

840   lines represent the melt compositional evolution modelling with 4% initial H_2O

841   content at 1.2 Kbar (wathet dashed line) and 3 Kbar (blue dotted line),

842   respectively.

843
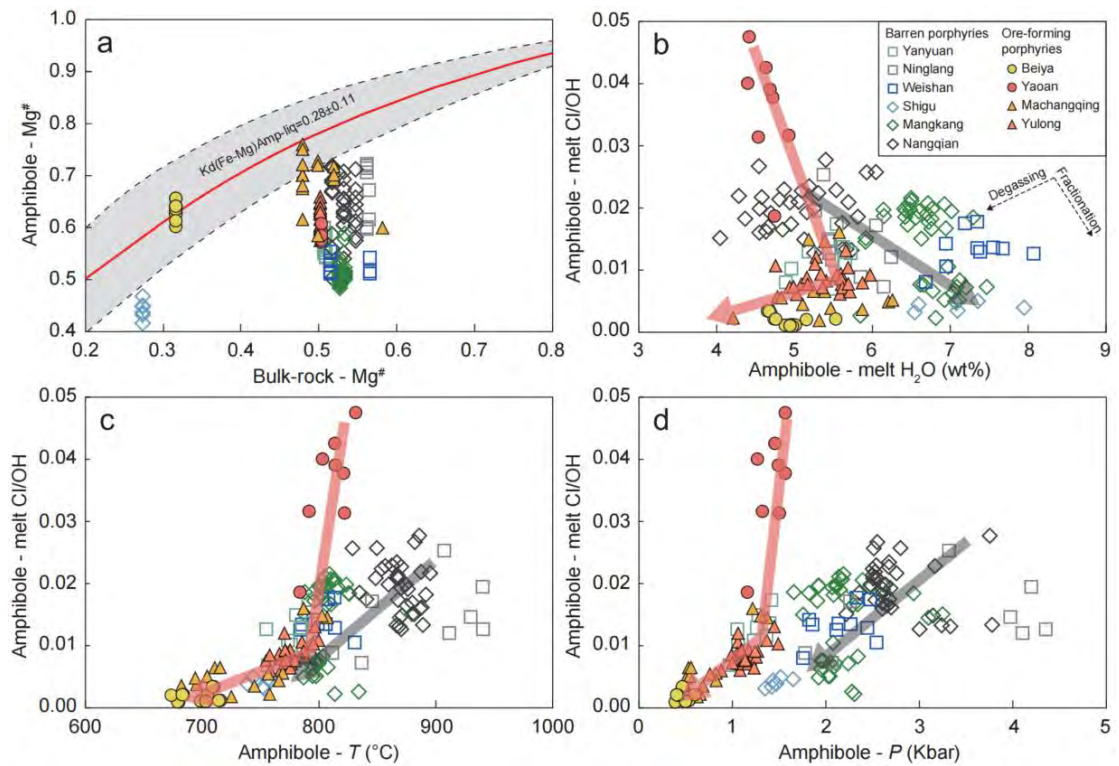
844

845 **Figure 4. a,** Test for equilibrium between amphibole and melt based on the Fe-

846 Mg exchange coefficient (K$_D$). K$_D$ values in the range of 0.28 ± 0.11 (Putirka,

847 2016). **b–d,** The calculated melt Cl/OH–H$_2$O, Cl/OH–T and Cl/OH–P,

848 respectively. Melt Cl/OH is calculated by amphibole compositions according to

849 Sato et al. (2005). The pink and gray thick lines illustrate continuous variation

850 trends of ore-forming and barren porphyries.

851

852
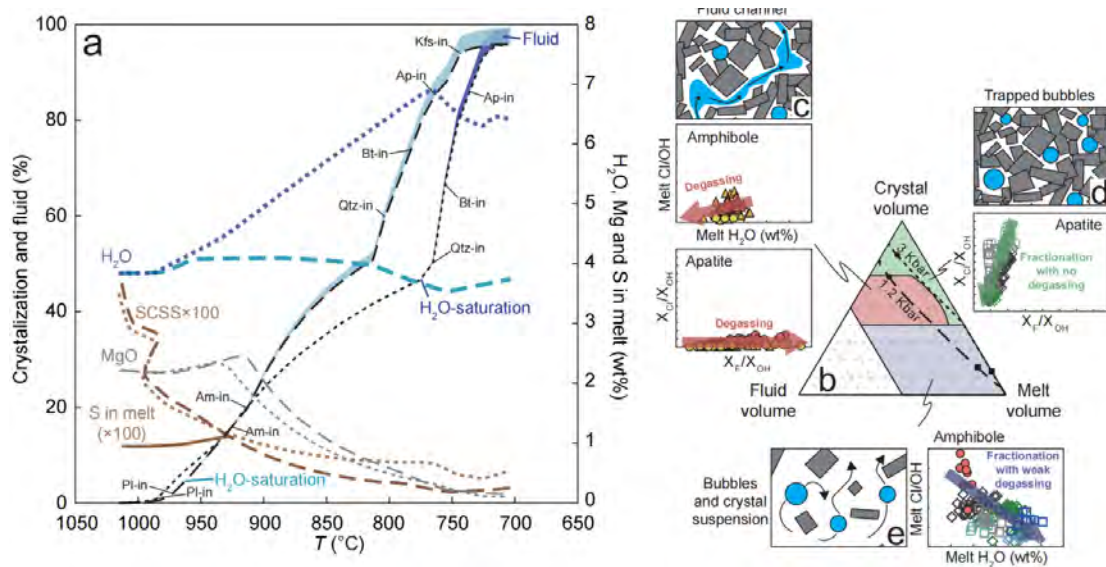
Figure 5a, Rhyolite-MELTS thermodynamic modelling for the ore-forming and

barren magmas in Sanjiang metallogenic belt. Summary of mineral phase and

extent of crystallization at 1.2 Kbar (black dashed line) and 3 Kbar (black dotted

line) for cooling and crystallizing. Residual melt MgO (gray) and H_2O (blue) are

shown at 1.2 Kbar (dashed lines) and 3 Kbar (dotted lines). The brown dashed and

dotted lines represent the trend of estimated sulfur concentration at sulphide

saturation (SCSS) at 1.2 Kbar and 3 Kbar, respectively. Meanwhile, the brown

continuous line traces the enrichment of sulfur within melts during magma

evolutions at 1.2 Kbar and 3 Kbar. Apatites have joined the crystallizing

assemblage before H_2O-saturation is achieved at both pressure conditions. **b–e,**

Models of fluid migration in shallow magma chambers according to Parmigiani et

al. (2017). The Bond number (Bo) is set as 0.5, which can describe the

competition between buoyancy and capillary stresses on fluid bubbles in the

hydrodynamics migration regime. The representative graphs around each model

illustrate how apatite and amphibole compositional trend relate to different fluid

43

868   migration processes. Black dots and squares represent the liquidus of apatite and

869   amphibole at different conditions, respectively.

870

871
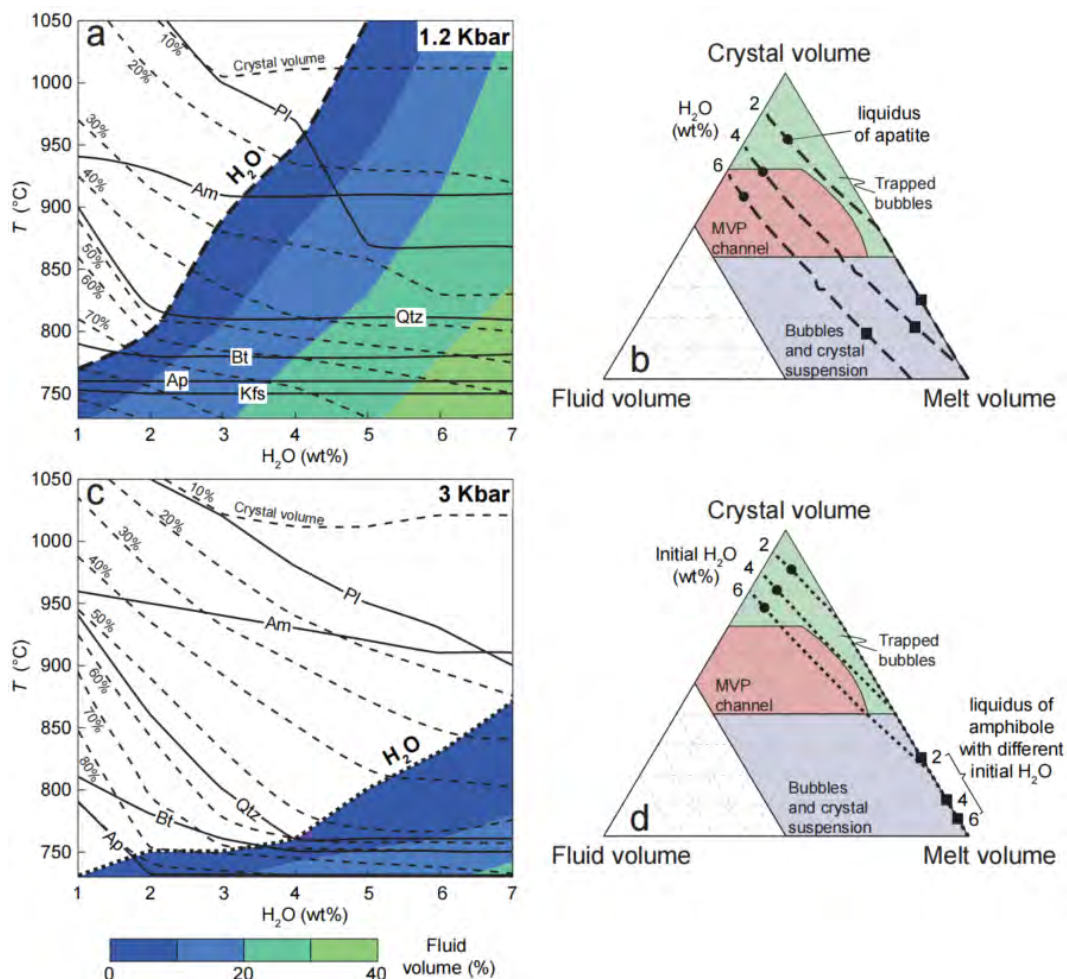
Figure 6a and c, Isobaric T–H_2O pseudosection for the ore-forming and barren

magmas in Sanjiang metallogenic belt with different initial H_2O contents. These

phase diagrams are constructed at constant pressures (1.2 Kbar and 3 Kbar,

respectively) and shows the influence of different initial H_2O contents at

temperatures of 730–1050 °C. The thin dashed lines show calculated crystal

volume proportion. The thick dashed and dotted lines represent the boundary of

H_2O-saturation at 1.2 and 3 Kbar, respectively. The filled colors represent the

volumes of exsolved fluids. The thin continuous lines are the liquidus of minerals.

b and d, Models of fluid migration in shallow magma chambers with different

initial H_2O contents according to Parmigiani et al. (2017). Black dots and squares

45

882   represent the liquidus of apatite and amphibole at different conditions,

883   respectively.

884
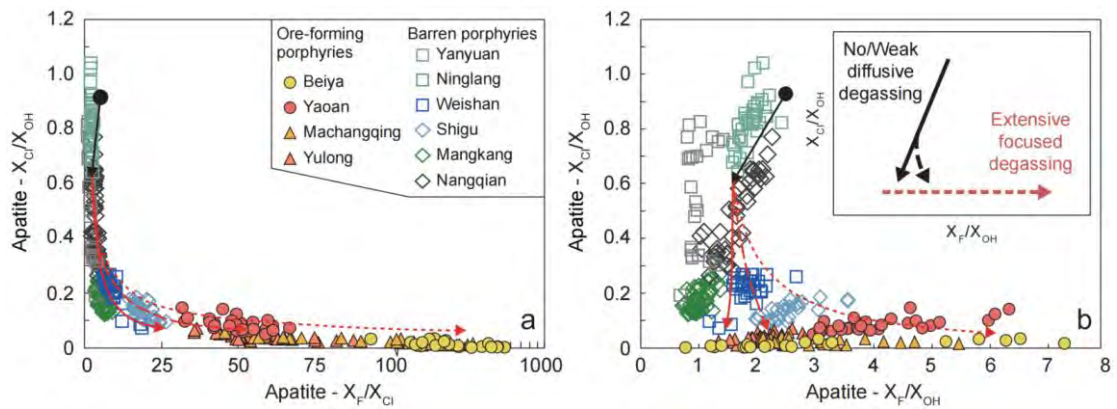
Figure 7. Volatile compositions of apatites from the adakite-like porphyries in

Sanjiang metallogenic belt. **a,** Apatite volatile compositions in X_{Cl}/X_{OH} versus

X_F/X_{Cl}. **b,** Apatite volatile compositions in X_{Cl}/X_{OH} versus X_F/X_{OH}. The

thermodynamic modelling of apatite compositional evolution is presented in a, b.

Apatite crystallization begins at the black point and continues to 50%

crystallization under H_2O-undersaturated condition according to the black arrow

(initial H_2O content is 4%; Dc/m F ≈ 0.99, Dc/m Cl ≈ 0.9 and Dc/m OH ≈ 0.01).

Then apatite compositional evolution continues in the red arrows to 90%

crystallization under H_2O-saturated condition. Line types illustrate the difference

between isobaric (0% H_2O loss; solid red line) H_2O-saturated crystallization and

polybaric H_2O-saturated crystallization with 0.05 wt% (dashed line) and 0.09 wt%

(dotted line) H_2O loss per 1% crystallization (total H_2O loss of 0%, 2 wt% and 3.5

wt%, respectively) according to the overall systems. The inset in **b** shows

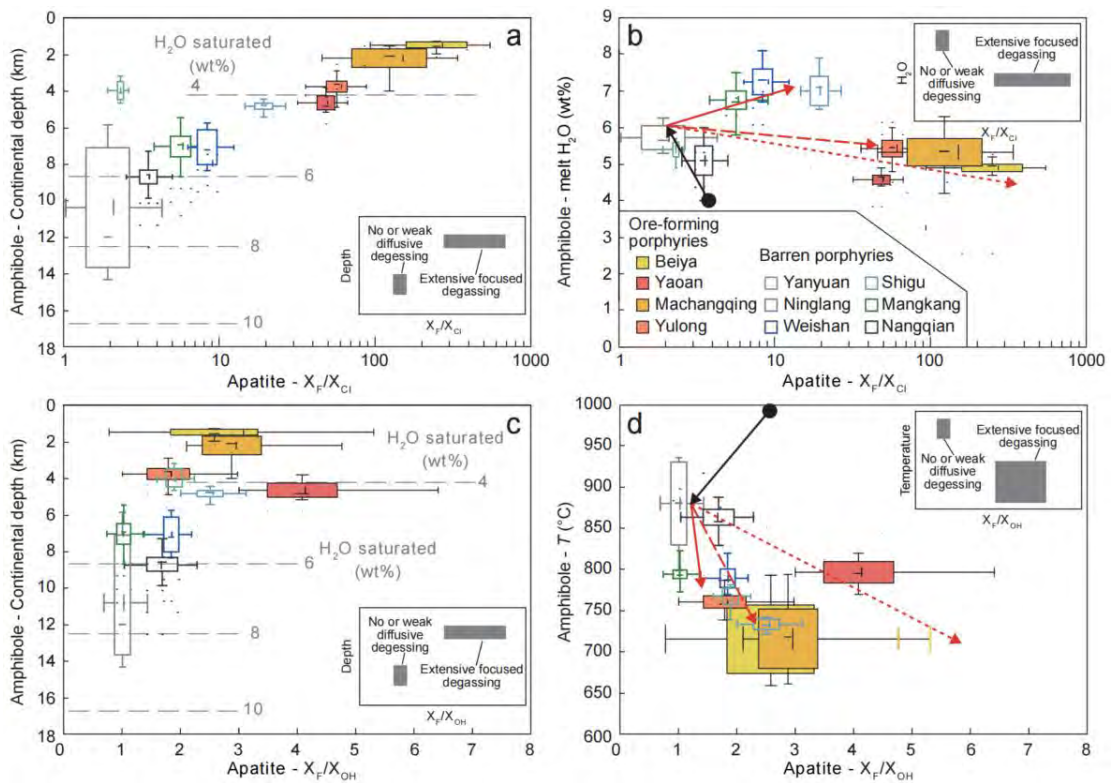compositional trajectories during no degassing (black solid line), weak diffusive

degassing (black dashed line) and extensive focused degassing (red dashed line)

according to X_{Cl}/X_{OH} versus X_F/X_{OH} ratios of apatites.

904

**Figure 8.** Box and whisker plots of volatile compositions of apatites and P–T–

H$_2$O calculated by amphiboles from the adakite-like porphyries in Sanjiang

metallogenic belt. Boxes show first to third quartile range with bars showing

extremes of data (excluding any outliers). Long and short lines in box show

square and mean value, respectively. The points outside boxes represent their

extremum values. The thermodynamic modelling of apatite compositional

evolution as for Figure 6. The gray dashed lines (in **a, c**) are H$_2$O solubility limits

(Ghiorso and Gualda, 2015; Collins et al., 2020). The grey squares in the insets

show different data features between no/weak diffusive degassing and extensive

focused degassing processes.

915

916
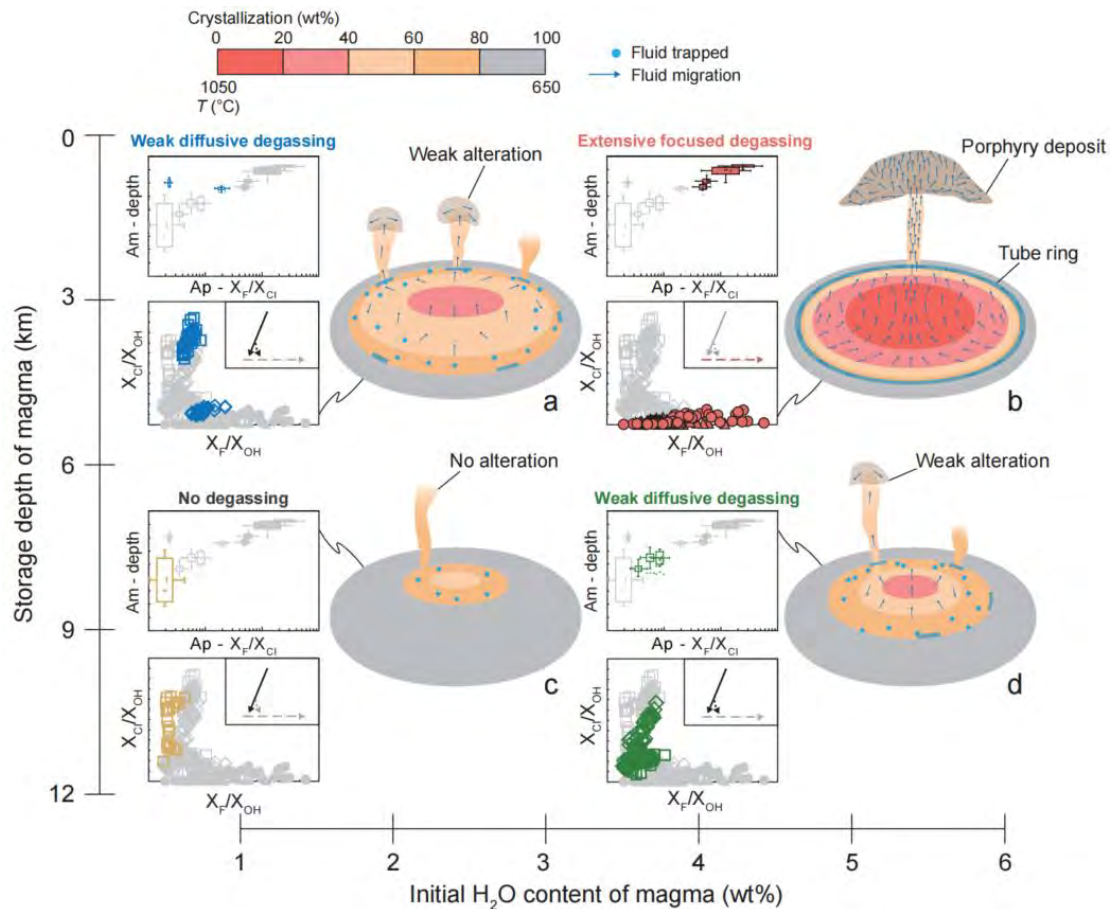
Figure 9. Classification of magma crystallization, fluid migration and degassing

patterns as a function of magma storage depths and initial H_2O contents. Three

principal mechanisms of degassing process can be distinguished as follows. Fluid

exsolution starts at the late trapped bubble stage with no degassing (c); A small

amount of degassing with weak fluid migration, forming discontiguous tube ring,

and most of exsolved fluids are trapped according to high crystallization (a, d);

Extensive fluid exsolution with intense migration and degassing with no trapped

fluids, and the integral tube ring controlling focused degassing. Efficient focusing

of fluids through a narrow window and cooling across a steep thermal gradient,

could make sulphide mineral precipitation in a limited rock volume, creating rich

mineralization, and form PCDs. (b). The representative graphs on the left

928   illustrate how apatite and amphibole compositional trend relate to different

929   degassing processes.

930